2D Materials

ACCEPTED MANUSCRIPT

Facile access to shape-controlled growth of WS_2 monolayer *via* environment-friendly method

To cite this article before publication: Lianqing Dong *et al* 2018 *2D Mater.* in press https://doi.org/10.1088/2053-1583/aae7eb

Manuscript version: Accepted Manuscript

Accepted Manuscript is “the version of the article accepted for publication including all changes made as a result of the peer review process, and which may also include the addition to the article by IOP Publishing of a header, an article ID, a cover sheet and/or an ‘Accepted Manuscript’ watermark, but excluding any other editing, typesetting or other changes made by IOP Publishing and/or its licensors”

This Accepted Manuscript is **© 2018 IOP Publishing Ltd**.

During the embargo period (the 12 month period from the publication of the Version of Record of this article), the Accepted Manuscript is fully protected by copyright and cannot be reused or reposted elsewhere.
As the Version of Record of this article is going to be / has been published on a subscription basis, this Accepted Manuscript is available for reuse under a CC BY-NC-ND 3.0 licence after the 12 month embargo period.

After the embargo period, everyone is permitted to use copy and redistribute this article for non-commercial purposes only, provided that they adhere to all the terms of the licence https://creativecommons.org/licences/by-nc-nd/3.0

Although reasonable endeavours have been taken to obtain all necessary permissions from third parties to include their copyrighted content within this article, their full citation and copyright line may not be present in this Accepted Manuscript version. Before using any content from this article, please refer to the Version of Record on IOPscience once published for full citation and copyright details, as permissions will likely be required. All third party content is fully copyright protected, unless specifically stated otherwise in the figure caption in the Version of Record.

View the article online for updates and enhancements.

This content was downloaded from IP address 129.108.9.184 on 18/10/2018 at 01:35

IOP Publishing Journal Title
Journal **XX** (XXXX) XXXXXX https://doi.org/XXXX/XXXX

Facile Access to Shape-controlled Growth of WS_2 Monolayer *via* Environment-Friendly Method

Lianqing Dong[1], Yuyan Wang[1*] [iD], Jiacheng Sun[1], Caofeng Pan[2], Qinghua Zhang[3], Lin Gu[3], Bensong Wan[1], Cheng Song[4], Feng Pan[4], Cong Wang[1], Zilong Tang[4], Junying Zhang[1*] [iD]

[1] Key laboratory of Micro-nano Measurement, Manipulation and Physics (Ministry of Education), Department of Physics, Beihang University, Beijing 100191, China
[2] Beijing Institute of Nanoenergy and Nanosystems, Chinese Academy of Sciences, Beijing 100083, China
[3] Beijing National Laboratory for Condensed Matter Physics Institute of Physics, Chinese Academy of Sciences, Beijing 100190, China
[4] School of Materials Science and Engineering, Tsinghua University, Beijing 100084, China

*E-mail: wangyy@buaa.edu.cn, zjy@buaa.edu.cn

Received xxxxxx
Accepted for publication xxxxxx
Published xxxxxx

Abstract

Two-dimensional materials with tailored morphologies exhibit distinctive shape-dependent properties especially in electrocatalysis and gas sensing, extending their applications in nanoelectronics. Atomic-layer tungsten disulfide (WS_2) stands out as a promising candidate, but the controllable synthesis of WS_2 still faces unavoidable obstacles, such as strict parameter requirements, low efficiency and serious pollution during the preparation. Here we report an elegant technique for growing homogeneous-luminescence WS_2 monolayer with desired shapes and developed electrochemical properties, through the improved chemical vapor deposition method with a semi-closed airflow environment. It is an effective, economic and especially environment-friendly approach with atmospheric-pressure and hydrogen-free condition, aiming at synthesizing high-quality and large-scale monolayer WS_2 crystals with only one heating zone. Compared with the existing methods, this one significantly minimizes the sulphur contamination to the environment and equipment, enabling the reuse of quartz tube and reducing the cost. More importantly, different shapes of WS_2 domains with high crystalline and excellent homogeneity of luminescent intensity are controllable by adjusting the growth temperatures. In addition to the good electrical transport performance of WS_2 monolayer, the WS_2 domains with different morphologies exhibit modulated properties for catalyzing the electrochemical hydrogen evolution. This systematic study on shape-controlled growth and shape-dependent electrochemical performances of WS_2 will further push forward their practical applications.

Keywords: WS_2 monolayer, shape evolution, semi-closed airflow, environment friendly, shape-dependent electrochemical performance

1. Introduction

Monolayer transition dichalcogenides (TMDs) have shown many fascinating properties such as the indirect-to-direct bandgap crossover, large spin-orbit coupling, strong quantum confinement and excellent luminescence properties [1−4], which make them attractive semiconductors in electronics [5], valleytronics [6−9], and optoelectronics [5,10]. As a member of TMDs family, atomically thin tungsten disulfide (WS_2) is a semiconductor analogue to MoS_2 with a direct band gap of ~2 eV [1,11−13]. It has stronger photoluminescence (PL) emission and exhibits stronger spin-orbit coupling and band splitting than other TMDs [14−16]. So great efforts are eagerly demanded to achieve large-area WS_2 monolayers, which are vital for their practical application in electronic and

 © xxxx IOP Publishing Ltd

Accepted Manuscript

optical devices [17,18]. Furthermore, two-dimensional materials with tailored morphologies interestingly exhibit shape-dependent properties and thus have potential application in building nanodevices [19−21]. Morphology management for modulating the properties of TMDs has attracted great interest for promising applications such as in electrocatalysis and optoelectronics [22]. It has been proved that hexagonal MoS_2 plays an important role in the chemical catalysis process or gas sensing compared with other shapes of MoS_2, and the dendritic MoS_2 is synthesized to study the twin defect derived growth mechanism [19,22]. So the controllable preparation of WS_2 samples with different morphologies is in great demand for the development of modern functional devices.

WS_2 has been less reported than other TMDs such as MoS_2 simply due to the difficulty in producing high-quantity samples through exfoliation or chemical vapor deposition (CVD) at relatively high temperature (more than 1000 °C). Recently, many efforts have been made on optimizing the parameters to obtain high-quality samples, such as introducing H_2, H_2S or water into the Ar_2 gas flow [23−26], adding heating sources to precisely control the volatilization of precursors [27−29], accurate control of the S introduction time [30,31] and so on. However, the controllable CVD growth of high-quality monolayer WS_2 still faces a great challenge, let alone the desired shapes. For instance, the positions of precursors are very critical that great care should be taken for each growth [30−32], and serious pollution to the environment and equipment would be caused by S vapour. As a result, the quartz tube must be changed frequently, which inevitably increases the cost.

In our method, we specially design a semi-closed airflow environment to solve these problems effectively. On one hand, the process of production is under a less-stringent condition so that precursors are not necessarily placed at identical position for each growth. And the equipment is simplified by using only one heating zone with atmospheric-pressure and hydrogen-free condition. On the other hand, there is no S release to the air, which minimizes the pollution. The quartz tube can be reused: the inside quartz tube was used more than 100 times and the outside quartz tube was never changed in our experiment, which greatly reduces the cost. More importantly, growth efficiency is increased in this method with a success rate of more than 80% for a large sample size of 250 μm, according to the general statistics. And the evolution of shapes with principles of crystal growth is clearly clarified with regard to different growth conditions. The standard triangles exhibit good electrical properties that the field-effect mobility of WS_2 monolayer is estimated up to 2.2 $cm^2/V{\cdot}s$ while the dense and small hexagon WS_2 domains are ideal catalysts for electrochemical hydrogen evolution. This provides a pretty effective approach to obtaining high-quality and shape-controlled samples in an efficient and environment-friendly way, which also proposes material basis for further study on shape-controlled properties and potential application.

2. Results and Discussion

The setup is designed to be much different from the previous reports [24,25,30,33]. As illustrated in Figure 1(a), we put a 2.5 cm-diameter sealed quartz tube with a 4 mm-diameter air went on the tube wall into the tube furnace. The precursors used here are powdered sulfur and tungsten trioxide. Both precursors are put into the thin quartz tube and heated simultaneously in the tube furnace. WO_3 is in the middle of the furnace and S is put a bit away from the furnace body. Both precursors are evenly dispersed into ceramic boats. The substrates used here are well cleaned SiO_2/Si wafers, which face the WO_3 precursor on the ceramic boat. Our method is much simplified because only one tube furnace with one single heating zone is used and the process is under the atmospheric pressure with flowing argon (blue arrow in Figure 1(a) indicates the direction of gas flow). The best growth empirical temperature to obtain standard triangle WS_2 flake is set to 1070 °C.

The dual-tube design is environmentally friendly, mainly due to the greatly reduced amount of precursors. Only 1% S and 1‰ WO_3 of the commonly reported amounts are needed to prepare the samples [30,32]. Combined with the dual-tube design, no exhaust emissions occurr during growth. As shown in Figure 1(b), both precursors are sublimated to gas and combined with each other in the inside tube as the temperature increases, followed by nucleating and growing on the substrate. Molecules move actively under the thermal motion and are fully utilized inside the quartz tube, which benefits from the semi-closed environment. Hence, only small amount of precursors are needed to realize high-quality and large-size growth, which greatly reduces the pollution. To highlight the environmental friendliness of the design, we also compare the pollution to quartz tube with the traditional CVD method (Figure S1). It is clear that the quartz tube in our work remains clean after repeated use for 100 times. Moreover, we also compared the optical images of samples obtained with new quartz tube and reused one (Figure S2). The sample quality and cleanliness keep the same, indicating the stability and low cost of this method.

To evaluate the quality of the grown WS_2 monolayer, images from optical microscopy, scanning electron Microscopy (SEM), Raman scattering spectrum and photoluminescence spectrum are presented. In Figure 1(c) and (d), the optical and SEM images exhibit the perfect triangular shape with sharp edges and smooth surfaces. The size of WS_2 domain edges can reach 250 μm and most of the domains are larger than 100 μm (More optical images are shown in Figure S3). Raman scattering spectrum excited by an excitation laser with a wavelength (λ_{ex}) of 532 nm is presented in Figure 1(e), which indicates the characteristic in-

Accepted Manuscript

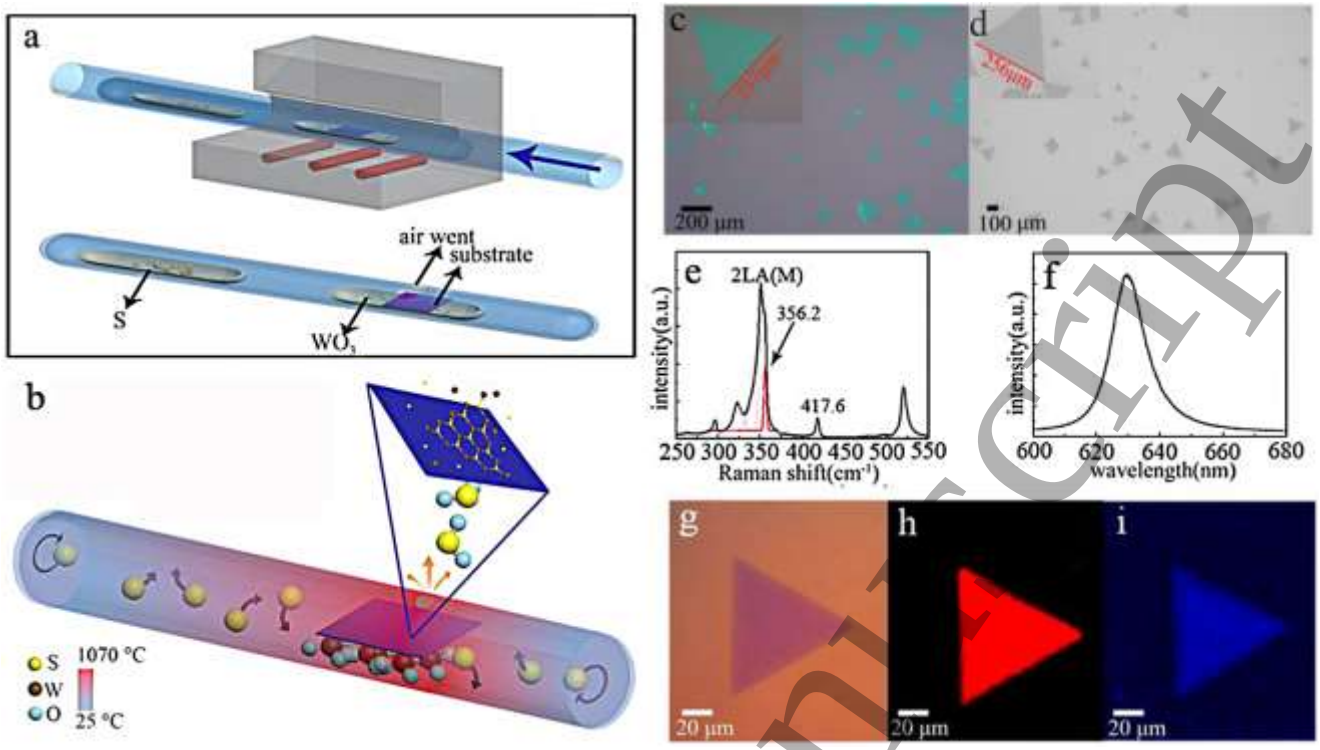

Figure 1 The schematic illustration of the CVD system and characterization of WS_2 triangular domains. (a) Schematic diagram of the CVD system for the WS_2 growth (top) and amplified schematic diagram of the inner quartz tube (bottom). (b) The schematic of growth process of monolayer WS_2. The blue quadrilateral outside the tube is the schematic enlarged SiO_2/Si substrate grown with WS_2. (c) Optical image of triangular WS_2 monolayer grown on SiO_2/Si substrate with the side length of 237 μm in the inset. (d) SEM image of triangular 1L-WS_2 with the side length of 256 μm in the inset. (e) Raman scattering spectrum and (f) PL spectrum excited in WS_2 domain. (g) WS_2 domains for Raman spectroscopy, PL spectrum, PL mapping and Raman mapping measurements. (h) PL mapping and (i) $A_{1g}(\Gamma)$ Raman mode intensity mapping excited in WS_2 domains.

plane vibrational ($E^1_{2g}(\Gamma)$) mode of W and S atoms and the out-of-plane vibrational ($A_{1g}(\Gamma)$) mode of S atoms at 356.2 cm^{-1} and 417.6 cm^{-1}, respectively. The frequency separation of 61.4 cm^{-1} between two modes and the strong 2LA(M) mode match the characteristic Raman scattering spectrum of single-layer WS_2 [15,29]. As shown in Figure 1(f), the strong PL peak is located at ~629 nm, which falls in the range of reported PL peak positions for monolayer WS_2 flakes [3,23]. In addition, PL mapping shows the homogeneity of the luminescent intensity, as displayed in Figure 1(h). High uniformity of the samples can also be verified by integrated intensity maps of Raman vibration modes (Figure 1(i)), based on the WS_2 domain shown in Figure 1(g). All these evidences prove that WS_2 domains obtained from this method are highly crystallized and uniform.

Interestingly, various WS_2 crystal geometries can also be obtained in our experiment, such as triangular, hexagonal, shrinking triangular, six pointed star-shaped domains. Different morphologies are easy to access at lower temperature, while the proportion of the standard triangular WS_2 flakes rises with temperature increased to 1070 °C (discussed in Figure S4). Uncovering the growth mechanism of WS_2 in this environmental-friendly method is the key to effectively control the growth process. We have designed a control experiment to explain the formation mechanism. Specially, very small amount of precursor WO_3 was put on a Si substrate centrally instead of scattering evenly on the bottom of the ceramic boat. The temperature was set at 950 °C to promote the formation of WS_2 with different morphologies. After reaction, there is a circular deposition on the covering substrate to the naked eyes, as presented in the inset of Figure 2(a). WS_2 domains show obvious annular regularities of distribution with the change of morphology and size, which are related to the position of WO_3. The schematic illustrations of the shape evolution are shown in Figure 2(a) with the optical images.The deposition area can be divided into several circles according to the distribution of different shapes. Figure 2(b) presents the four corners of the growth area on the substrate observed under low magnification, illustrating the divergent shapes (also see Figure S7). Domains around the center are bigger than 100 μm with standard triangular morphology (Figure 2(c)). At the next circle of the deposition area, most of the WS_2 domains present shrinking triangles with side length of 50−100 μm as shown in Figure 2(d). As the location moves further from the center (Figure 2(e)), some of the domains transform into irregular hexagon with the size less

Accepted Manuscript

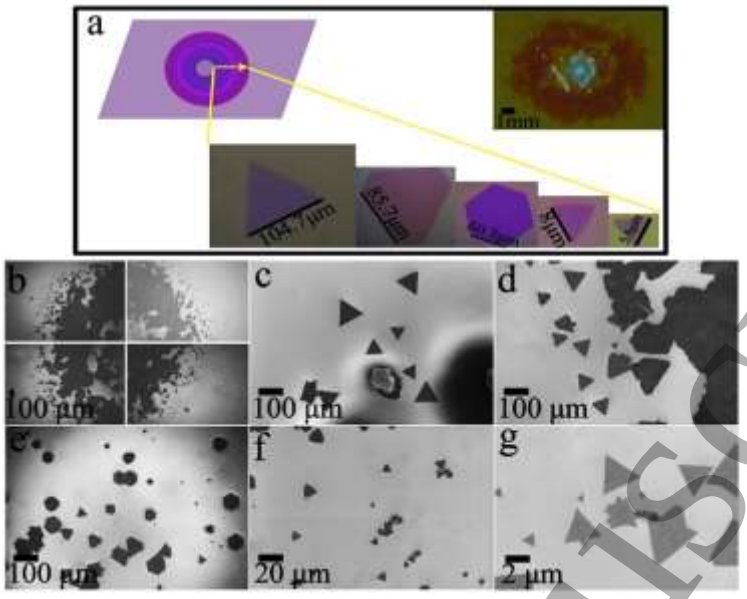

Figure 2 Shape and size evolution of WS_2 domains at different positions. (a) The schematic segmentation and their typical optical images. The inset is the picture of WS_2 on substrate to the naked eyes. (b) SEM images of four corners of deposition area in low magnification. (c−g) SEM images of different morphology of WS_2 along the distance increasing from the center.

than 50 μm. While for the outer circle, most of them become edge-smooth triangles in Figure 2(f) with the length of about 20 μm. Finally, a few domains become triangles but with zigzag sides less than 10 μm. In all, the morphology and size of WS_2 domains present the obvious regional distribution regularity.

This phenomenon can be elucidated by the mechanism of crystal growth. WS_2 domains, the two-element system, have two types of zigzag edge terminations. The different growth rates at two types of crystal faces determine the growth morphology, which has been verified by the analogous growth mechanism of MoS_2 that the slowest growing faces become the largest, while the rapidly growing faces either become smaller or disappear [34,35]. For example, when WS_2 is grown under an extreme condition rich in S, W terminations tend to grow quickly, leading to the larger S termination. So the final shape will be related to the growing rate of different edge terminations, which are further determined by the amount of volatile precursors and different atomic ratio. To be specific in our experiment, the concentration gradient of S vapor in reaction area can be neglected, since the S source completely volatilized and distributed evenly throughout the reaction process. So the amount of volatile WO_{3-x} varies in different locations during the reaction process, leading to a circular gradient distribution in the reaction area. The cause of concentration gradient of W is mainly due to the centralized placement mode of precursor WO_3 and the relatively low heating temperature which can not evaporate WO_3 fully.

Accordingly, the amount of two volatile precursors W: S in the growth location are considered to be the key factors in morphology formation, which influence the growth rate of different crystal faces. Bigger triangles with straight and sharp sides are formed in the center, due to the sufficient W source. So the S terminations grow quickly leading to the triangle shapes. With the increase of distance from the center, shrinking WS_2 domains appear as the amount of W source decreases and the growth speed of S zigzag face decreases. The hexagon dominant region indicates that the two terminations have similar growth speed, corresponding to the decreasing amount of W in this annular region. For domains in next outer circle shown in Figure 2(f), most domains turn back to triangles due to the lack of W atoms where W terminations grow quickly.Finally, triangles with small size grow in the edge region with zigzag sides, consistent

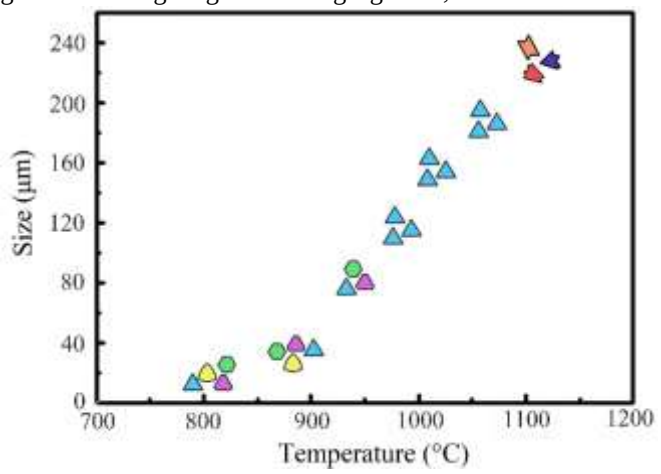

Figure 3 Shape and size evolution schematic diagram of WS_2 flakes with respect to growth temperature.

Accepted Manuscript

with the previous research that S terminations always exhibit zigzag edges [36]. This allows us to easily identify crystal orientation in optical images. The proposed mechanism here is also supported by similar phenomena which have been identified in the growth process of MoS_2, where different Mo: S ratio is the key origin for the varying domain shapes along the gas flow direction [34], under different temperatures [37] or with different amount of precursor S [38].

Quantitative stoichiometries for each WS_2 flake in different shapes were detected using energy-dispersive X-ray spectroscopy (EDS) (Figure S8). The S/W ratio are 1.977 for the standard triangle, 2.06 for standard hexagon and 2.29 for edge-smooth triangle respectively. It shows the trend of increasing S/W ratio, supporting the growth mechanism discussed above. X-ray photoemission spectroscoy (XPS) was also adopted to confirm the regularity (Figure S9). Three peaks at 32.99, 35.18, and 37.82 eV are attributed to the W $4f_{7/2}$, W $4f_{5/2}$, and W $5p_{3/2}$, respectively. The peaks with binding energy of 162.46 and 163.64 eV come from S $2p_{3/2}$ and S $2p_{1/2}$ respectively, consistent with the values reported elsewhere [39,40,41]. The calculated stoichiometric ratio of S/W is increased as the standard triangles turn to hexagons, agreeing well with data from EDS.

Accordingly, relatively higher temperature crucially contributes to an increase of the proportion of W with respect to S in the growth region by facilitating the surface diffusion of WO_3, which makes the triangles take shape quickly by accelerating the termination growth. In contrast, lower temperature lacks a sufficient vapor pressure for growth and reduces the evaporation amount of WO_3 at different levels, so there are more possibilities for different shapes of WS_2 with the change of W: S ratio. To make it more intuitive, Figure 3 summarizes the shape and size evolution schematic diagram of WS_2 flakes with respect to growth temperatures. It is clearly shown that various kinds of shapes of WS_2 domains appear in the relatively low temperature (range from 750 °C −1000 °C). As the temperature is higher than 1000 °C, the proportion of standard triangular domains increases dramatically. Different shapes of polycrystalline WS_2 domains appear when the temperature is higher than 1070 °C. The size of WS_2 domains increases almost linearly with increasing temperature. This shape-evolution diagram provides an effective way to obtain desired shape and size of WS_2 domains simply by adjusting heating temperatures, which can be used as a practical guide for producing desired samples.

WS_2 domains in different shapes show uniform luminous properties. WS_2 flakes including standard triangle, butterfly-shaped mirror twin island, shrinking triangular domain, hexagonal domain, and edge-smooth triangles have been investigated (Figure 4(a) – (e)). It is surprising that monolayer WS_2 domains in different shapes all show great homogeneity of luminescent intensity, except for slight edge PL deterioration which might be passivation incurred by impurities or localized oxidation in the air [23,42]. Although relatively homogeneous luminescence can be obtained in other 2D materials such as MoS_2, $MoSe_2$ and WSe_2 [43–46], uniform luminescence is uncommon in WS_2 due to crystal imperfections. Obvious discrete segmentation of PL emission intensity is often observed in hexagon WS_2 domains. PL enhancement is shown in the edge of standard triangular and non-triangular domains usually show poorer luminescence properties than triangular ones [47–49]. Hence, the PL homogeneity of WS_2 domains in different morphologies indicates their high crystallinity. The high quality of the samples in all morphologies can also make the preparation and practical application more flexible. Furthermore, we also investigate the stability of the deposited WS_2 monolayers. Different from the perfect triangles which are deemed to be stable, it should be noted that intersecting WS_2 flakes evolved from more than one nucleus have less stability. Figure 4(f) and (g) display the PL intensity maps before and after a mild oxidation process in air for a month. An obvious reduction of PL intensity in the position of grain boundary is shown. We further examine the atomic structure of WS_2 grain boundaries using aberration-corrected annular dark-field scanning transmission electron microscopy (ADF-STEM). The mirror twin boundary is clearly shown in Figure 4(h) where the atomic arrangement on either side of grain boundary is mirrored. Different orientations on both sides of the grain boundary break the structural periodicity, thus the presence of nonhexagonal ring structures causes the instability because the

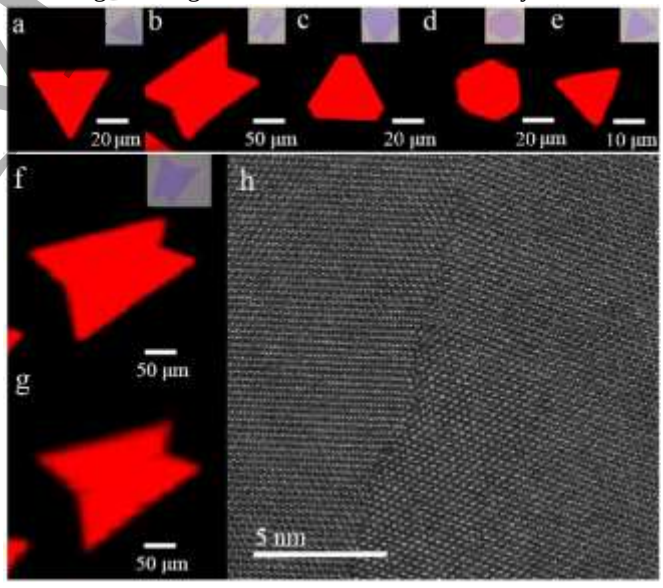

Figure 4 PL mapping of WS_2 flakes in different shapes. PL mapping of (a) standard triangle, (b) butterfly-shaped mirror twin domain, (c) shrinking triangular domain, (d) hexagonal domain and (e) edge-smooth triangular domain. (f) PL intensity map of WS_2 domain in butterfly shape, (g) PL intensity map of WS_2 domain in butterfly shape after a mild oxidation process in air for a month. (h) High-resolution ADF-STEM image of mirror twin boundary.

Accepted Manuscript

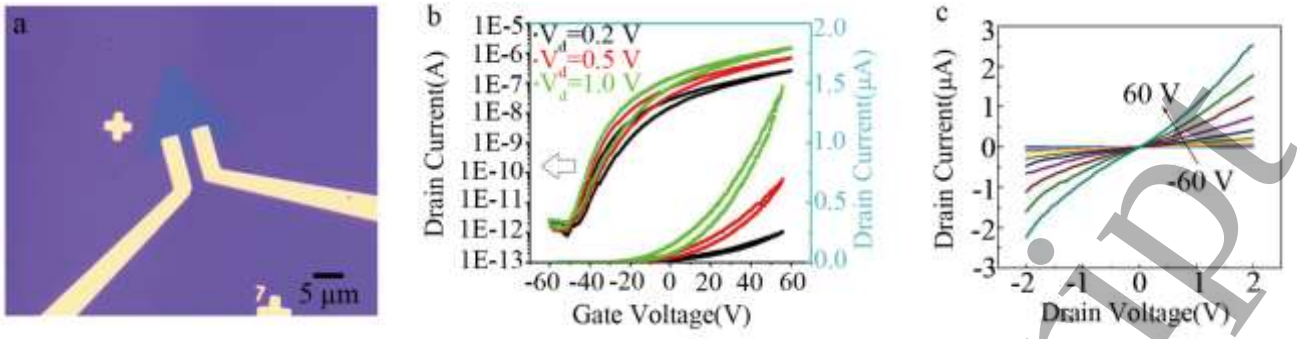

Figure 5. FET device fabricated by as-synthesized monolayered triangular WS_2. (a) Optical micrograph of the FET device fabricated by as-synthesized monolayered triangular WS_2 with Cr/Au contacts on SiO_2/Si substrates. (b) Transport characteristics of the FETs fabricated on as-grown WS_2 on a linear scale (right y-axis) and a log scale (left y-axis). (c) Output characteristics (Ids-Vds) of the WS_2 FET as a function of back-gate voltage ranging from -60 to +60 V in steps of 10 V.

degradation occurs firstly at the grain boundary. Furthermore, the longer the placement time, the more obvious the luminescence attenuation becomes at grain boundary (Figure S10). It is interesting that clear PL suppression can also be found along lines from nucleation sites to sharp corners (Figure S10 (j) and (k)), which may be caused by the released strain introduced during placement and further research is still needed.

Now we turn towards the electrical performance of the WS_2 monolayers, as a basis for device operation. The bottom-gated WS_2 monolayer transistors were fabricated on 285 nm SiO_2/Si, with Cr (10 nm)/Au (40 nm) electrodes. Figure 5(a) shows an optical micrograph with WS_2 monolayer consisting of two-terminals structure with a channel length and width both of 2 μm. Figure 5(b) presents the transport characteristics of the corresponding Field-effect transistor (FET) device on a linear (right y-axis) and log scale (left y-axis). The WS_2 monolayer shows n-type behavior and a high on-off current ratio exceeding 10^6. The field-effect electron mobility of the devices was extracted from the linear region of the transfer properties using the equation $\mu=[dI_d/dV_{bg}] \times [L/(WC_gV_d)]$ [50], where L, W, I_d and V_{bg} are the channel length, width, drain current and the gate voltage, respectively. C_g, estimated to be ~10 μF/cm^2, is the area capacitance between the channel and the back gate per unit area ($C_g = \varepsilon_0\varepsilon_r/d$, where ε_0 is the permittivity of free space, $\varepsilon_r = 3.9$, and $d = 285$ nm). The field-effect mobility of monolayer WS_2 is estimated up to 2.2 cm^2/V·s, which is higher than many other reported WS_2 samples [33,51–52]. The superior electrical performance of our single-layer WS_2 demonstrates its high quality and low defect. As shown in Figure 6(c), the output characteristics of WS_2 FET were measured by sweeping various back gate voltage (−60 to +60 V) in steps of 10 V. The almost linear output curves of WS_2 indicates the Ohmic contact between the monolayer WS_2 and the Cr/Au electrode at the source and drain parts. The output and transfer characteristics of the monolayered WS_2 reflect that its high degree of crystallinity gives rise to its excellent electrical characteristics. Admittedly, TMDs with hexagonal or other morphologies contain relatively more defects that are mainly due to the vacancies, which are not suitable for FET fabrication [19,47]. However, beneficial from the higher distribution of active sites in the whole basal plane when compared with other shapes, a higher catalytic activity is expected in hexagonal WS_2 [19].

In order to explore the effect of different morphologies on their electrochemical properties, the performances of hydrogen evolution reactions (HER) are studied by adopting WS_2 as catalyst. WS_2 nanosheets show clear shape-dependent catalytic activity. In our study, a three-electrode system was used to evaluate the HER electrocatalytic performances of WS_2 samples, using 0.5 M H_2SO_4 electrolyte and a scan rate of 5 mV/s. Samples were transferred onto the glassy carbon electrode for tests. Four WS_2 samples of discrete triangular WS_2 flakes, polycrystalline WS_2 connected films, discrete hexagon WS_2 flakes and discrete hexagon WS_2 flakes with higher density were selected as HER catalysts. These four samples are obtained at 980 °C, 1200 °C, 840 °C and 825 °C, respectively. As shown in Figure 5 (a), there is a significant improvement in electrocatalytic performance when we use the hexagonal WS_2 flakes as the catalyst (black curve, sample C) compared with triangular WS_2 flakes and polycrystalline WS_2 film. When the density of WS_2 flakes is increased, best performance is shown in Figure 5 (a) with the red curve (sample D). It has a low overpotential value of 276 mV versus reversible hydrogen electrode (RHE) for a current density of 10 mA/cm^2 with an onset potential of 87 mV. The D electrode has a Tafel slope of 95 mV/dec, which is superior to the previous CVD ones [53]. To probe the stability and durability of the electrode, continuous CV was performed in 0.5 M H_2SO_4 solution (Figure 5(b)). As can be observed, the polarization curve of the D electrode is pretty stable with slight improvement after 1000 cycles. We can infer that WS_2 flakes

Accepted Manuscript

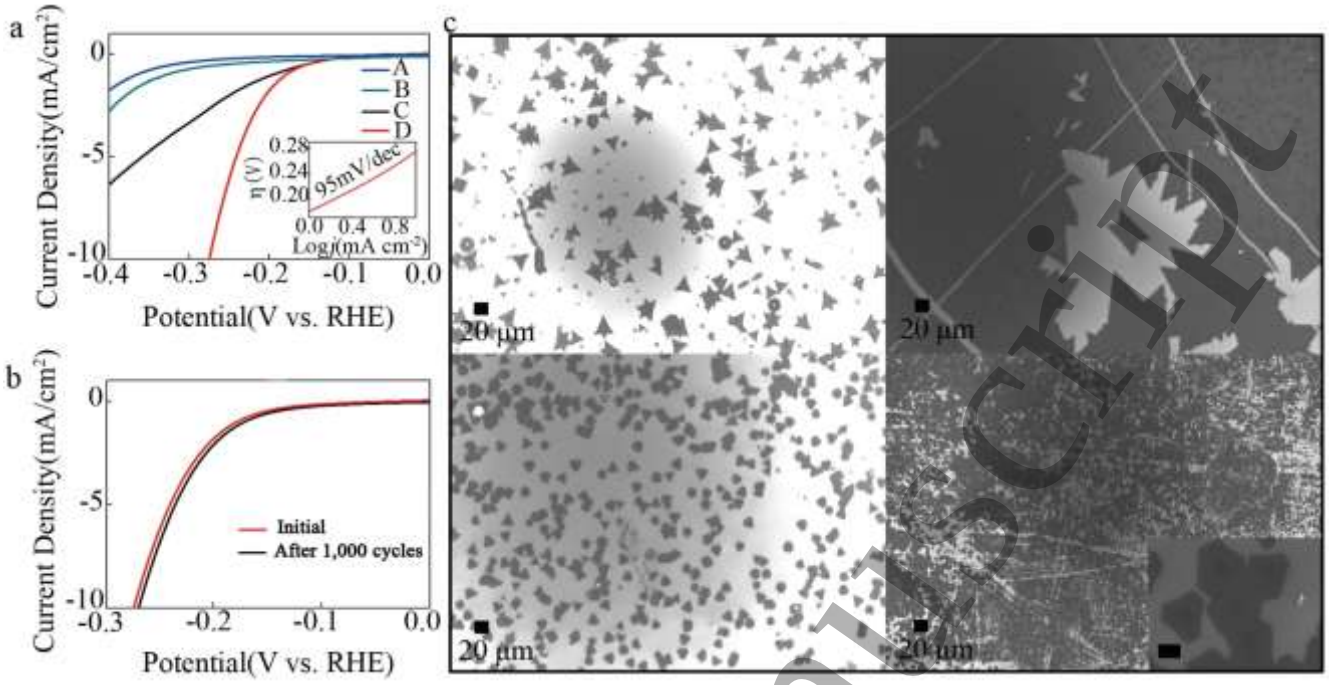

Figure 6. HER activity characterization. (a) Polarization curves of WS_2 flakes in four different morphologies (sample A: discrete triangular WS_2 flakes, sample B: polycrystalline WS_2 connected films, sample C: discrete hexagon WS_2 flakes, sample D: discrete hexagon WS_2 flakes with higher density). The inset gives corresponding Tafel plot . (b) Polarization curves of sample D in the 1st cycle and after 1000 CV cycles. (c) SEM images of samples A, B, C and D. The scale bar in the inset is 2 μm.

with hexagonal morphology has more catalytic active sites compared with standard triangle, leading to superior electrochemical properties. It will provide a new approach towards improving the catalytic performance, even for other two-dimensional materials (MoS_2, TaS_2 etc) obtained by CVD method. Consequently, the shape-controlled growth of WS_2 in this work presents great advantages on achieving desirable shapes of WS_2 monolayers for different device applications.

3. Conclusion

A facile CVD method, within a semi-closed environment, has been proposed to prepare high-quality and large-scale WS_2 monolayers. The experiment was conducted under atmospheric pressure with one heating zone, and proved to be highly effective, cost-saving and environment-friendly. We emphasize that the temperature plays an essential role in the formation of high-quality monolayer TMDs and clarify the growth mechanism related to different size and shape of WS_2. Shape evolution of WS_2 domains has been clearly demonstrated by establishing a gradient of WO_3 precursor concentration intentionally. It is concluded that the ratio of W: S is the decisive factor to influence the shape evolution and it's pretty easy to control in this semi-closed growth environment with less-stringent condition. On the basis of the results, a shape-controlled diagram is developed, which can be used as a practical guide for the growth of domains with desired shapes. More importantly, samples with different morphologies have different electrochemical properties, which provides material basis in various practical applications. In addition to the better electrical transport characteristics for monolayered triangular WS_2, the hexagon WS_2 flakes exhibit superior properties on hydrogen evolution catalysis.This growth method and growth mechanism could be transplantable to other TMD materials, which provide guidance for preparing high-quality two-dimensional materials with different shapes in an effective and environment-friendly way.

4. Method

4.1 Growth of WS_2 in semi-closed environment

The single-layer WS_2 were grown on the Si substrates with 280 nm SiO_2 on its surface. The furnace used here is a simple tube furnace with only one heating zone and the constant temperature area of 20 cm. 2D WS_2 are synthesized with the precursors of tungsten trioxide (WO_3, 99.95%, Alfa Aesar) and Sulfur (S, 99.99%, Alfa Aesar) in atmospheric pressure CVD (APCVD) using argon as the carrier gas. 1 mg WO_3 and 10 mg S were used in each growth process. Both precursors were contained in ceramic boat and put into a quartz tube with a tiny hole on the tube wall. When the quartz tube was put into the furnace, WO_3 was placed exactly at the center of the

Accepted Manuscript

furnace heating zone, and S was placed about 18−20 cm from the heating center outside the furnace body so that it can be radiated by the emitting heat. The substrates were placed face-down above the WO_3. Before heating, the tube furnace was flushed three times by argon gas. Then the argon flow rate was reduced to 100 sccm. The growth was carried out at the temperature of 1070 °C with the heating rate of 15 °C/min, then the holding time was kept for 15 min. Finally, the furnace was cooled naturally.

4.2 ADF-STEM sample preparation

The as-grown sample was first spin-coated with PMMA resist (AR-P 679.04) at 1000 rpm for 60s and then baked at 180 °C for 1 h. The sample was put into a 15 M KOH solution in a water bath at 50 °C until the PMMA/WS_2 film was thoroughly separated from the substrate. Then the film was cleaned in the DI water for several times. For ADF-STEM characterization, the PMMA/WS_2 was transformed onto the holy Quantifoil grids and left to dry overnight in air. Then the sample was baked at 150 °C for 15min to improve sample adhesion. Finally, the substrate was put into acetone solution for 5min to remove PMMA.

4.3 Characterization of samples

Raman and PL spectra, including corresponding mappings were measured via an Andor 500i spectrograph with a 532 nm laser and with the power of 1 mW. The Raman curves were taken using a 1800 lines mm^{-1} grating for 10 s, while the PL curves were taken with 600 lines mm^{-1} grating for 10 s. The Raman and PL mapping were conducted on the same instrument with the same laser line. The size and shape of samples were observed on an optical microscopy and a field emission scanning electron microscope (Zeiss) operating at 5 kV. ADF-STEM imaging was conducted using a JEM-ARM200F.

4.4 Device Fabrication

Monolayer WS_2 flakes grown by CVD were transferred onto a 285 nm SiO_2/Si substrate. The transfer process is consistent with 4.2. PMMA resist (AR-P 679.04) was coated under 3600 r/min and baked at 180 °C for 2 min. JSM-6460LV electron-beam lithography (EBL) system was used to pattern bond pads on the layer of PMMA resist. The samples were subsequently patterned with the developer solution (AR600-56) for 86s and the developer solution residual was washed in isopropanol for 30s. Then, a 10 nm Cr and 30nm Au layer were deposited by electron beam evaporation. For the lift off process to finally define drain/source electrodes, acetone, and ethyl alcohol were used, respectively. All output and transfer characteristics were characterized by using a semiconductor parameter analyzer (KEITHLEY, 4200B) at room temperature.

4.5 Electrochemical Characterization

Electrochemical measurements was performed in 0.5 M H_2SO_4 using a standard three-electrode configuration by an electrochemical analyzer (model CHI660E) with a carbon rod as counter electrode. The Ag/Agcl electrode was used as the reference. WS_2 domains were transferred onto the glassy carbon piece (1cm*1cm) as the working electrode. Nitrogen gas was bubbled into the electrolyte throughout the experiment. Electrochemical characterizations of the samples were performed using linear sweeping with a scan rate of 5 mV/s. in 0.5 M H_2SO_4, E(RHE) = E(Ag/Cl) + 0.202 V.

Acknowledgements

This project is financially supported by National Natural Science Foundation of China (Grant 51672106 and 51601006) and the State Key Laboratory of New Ceramic and Fine Processing Tsinghua University (No. KF201602).

ORCID iDs

Yuyan Wang iD https://orcid.org/0000-0002-6369-7103
Junying Zhang iD https://orcid.org/0000-0002-4860-8774

References

[1] Splendiani A, Sun L, Zhang Y, Li T, Kim J, Chim C Y, Galli G, Wang F 2010 *Nano Lett.* 10 1271−1275
[2] Eda G, Yamaguchi H, Voiry D, Fujita T, Chen M, Chhowalla M 2011 *Nano Lett.*11 5111−5116
[3] Zhao W, Ghorannevis Z, Chu L, Toh M, Kloc C, Tan P H, Eda G 2013 *ACS Nano* 7 791−797
[4] Mak K F, Lee C, Hone J, Shan J, Heinz T F 2010 *Phys. Rev. Lett.*105 136805
[5] Wang Q H, Kalantar-Zadeh K, Kis A, Coleman J N, Strano M S 2012 *Nat. Nanotechnol.* 7 699−712
[6] Mak K F, He K, Shan J, Heinz T F 2012 *Nat. Nanotechnol.* 7 494−498
[7] Cao T et al 2012 *Nat. Commun.*3 887
[8] Xiao D, Liu G B, Feng W, Xu X, Yao W 2012 *Phys. Rev. Lett.*108 196802
[9] Salle G et al 2012 *Phys. Rev. B.* 86 081301(R)
[10] Perea-López N et al 2013 *Adv. Funct. Mater.* 23 5511−5517
[11] Frey G L, Tenne R, Matthews M J, Dresselhaus M S, Dresselhaus G 1998 *J. Mater. Res.*13 2412−2417
[12] Ballif C, Regula M, Schmid P E, Remškar M, Sanjinés R, Lévy F 1996 *Appl. Phys. A: Mater. Sci. Process.* 62 543−546
[13] Cong C, Shang J, Wu X, Cao B, Peimyoo N, Qiu C, Sun L, Yu T 2014 *Adv. Opt. Mater.* 2 131−136
[14] Gutiérrez H R, Perea-López N, Elías A L, Berkdemir A, Wang B, Lv R, López-Urías F, Crespi V H, Terrones H, Terrones M 2013 *Nano Lett.* 13 3447−3454
[15] Zeng H et al 2013 *Sci. Rep.*3 1608
[16] Zhu Z Y, Cheng Y C, Schwingenschlögl U 2011 *Phys. Rev. B* 84 153402
[17] Ovchinnikov D, Allain A, Huang Y S, Dumcenco D, Kis A 2014 *ACS Nano* 8 8174−8181
[18] Lan C, Li C, Yin Y, Liu Y 2015 *Nanoscale* 7 5974−5980

Accepted Manuscript

[19] Zhang G, Wang J, Wu Z, Shi R, Ouyang W, Amini A, Chandrashekar B N, Wang N, Cheng C 2017 *ACS Appl. Mater. Interfaces.* 9 763-770
[20] Fan L, Zou J, Li Z, Li X, Wang K, Wei J, Zhong M, Wu D, Xu Z, Zhu H 2012 *Nanotechnol.* 23 115605
[21] Jun Y-W, Choi J S, Cheon J 2006 *Angew. Chem. Int. Ed.*45 3414−3439
[22] Wang J et al 2018 *ACS Nano* 12 635−643
[23] Zhang Y et al 2013 *ACS Nano* 7 8963−8971
[24] Kang K N, Godin K, Yang E H 2015 *Sci. Rep.* 5 13205
[25] Sheng Y, Tan H, Wang X, Warner J H 2017 *Chem. Mater.* 29 4904−4911
[26] Kastl C, Chen C T, Kuykendall T, Shevitski B, Darlington T P, Borys N J, Krayev A, Schuck P J, Aloni S, Schwartzberg A M 2017 *2D Mater.* 4 021024
[27] Peimyoo N, Shang J, Cong C, Shen X, Wu X, Yeow E K L, Yu T 2013 *ACS Nano* 7 10985−10994
[28] Thangaraja A, Shinde S M, Kalita G, Tanemura M 2016 *Appl. Phys. Lett.* 108 053104
[29] Berkdemir A et al 2013 *Sci. rep*. 3 1755
[30] Rong Y, Fan Y, Leen Koh A, Robertson A W, He K, Wang S, Tan H, Sinclair R, Warner J H 2014 *Nanoscale* 6 12096−12103
[31] Sun L, Leong W S, Yang S, Chisholm M F, Liang S J, Ang L K, Tang Y, Mao Y, Kong J, Yang H Y 2017 *Adv. Funct. Mater*. 27 1605896
[32] McCreary K M, Hanbicki A T, Jernigan G G, Culbertson J C, Jonker B T 2016 *Sci. Rep.*6 19159
[33] Xu Z-Q et al 2015 *ACS Nano* 9 6178−6187
[34] Wang S, Rong Y, Fan Y, Pacios M, Bhaskaran H, He K, Warner J H 2014 *Chem. Mater.*26 6371−6379
[35] Cheng J, Jiang T, Ji Q, Zhang Y, Li Z, Shan Y, Zhang Y, Gong X, Liu W, Wu S 2015 *Adv. Mater.* 27 4069−4074
[36] van der Zande A M, Huang P Y, Chenet D A, Berkelbach T C, You Y, Lee G H, Heinz T F, Reichman D R, Muller D A, Hone J C 2013 *Nat. Mater.*12 554−561
[37] Yang S Y, Shim G W, Seo S B, Choi S Y 2017 *Nano Res.*10 255−262
[38] Najmaei S, Liu Z, Zhou W, Zou X, Shi G, Lei S, Yakobson B I, Idrobo J C, Ajayan P M, Lou J 2013 *Nat. Mater.*12 754−759
[39] Behura S, Chang K-C, Wen Y, Debbarma R, Nguyen P, Che S, Deng S, Seacrist M R., Berry A V 2017 IEEE Nanotechnol. Mag. 33−38
[40] Song J-G et al 2013 ACS Nano 7 11333−11340
[41] Mao X, Xu Y, Xue Q, Wang W, Gao D 2013 Nanoscale Res. Lett. 8 430
[42] He Z, Wang X, Xu W, Zhou Y, Sheng Y, Rong Y, Smith J M, Warner J H 2016 *ACS Nano* 10 5847−5855
[43] Bilgin L et al 2015 *ACS Nano* 9 8822-8832
[44] Chen J et al 2016 *Adv. Sci.*3 1600033
[45] Shaw J C, Zhou H, Chen Y, Weiss N O, Liu Y, Huang Y, Duan X 2014 *Nano Res.*7 511-517
[46] Liu B, Fathi M, Chen L, Abbas A, Ma Y, Zhou C 2015 *ACS Nano*. 9 6119-6127
[47] Jeong H Y, Jin Y, Yun S J, Zhao J, Baik J, Keum D H, Lee H S, Lee Y H 2017 *Adv. Mater*.29 1605043
[48] Sheng Y et al 2017 *ACS Appl. Mater. Interfaces* 9 15005−15014
[49] Kim M S, Yun S J, Lee Y, Seo C, Han G H, Kim K K, Lee Y H, Kim J 2016 *ACS Nano* 10 2399-2405
[50] Li S, Wang S, Tang D-M, Zhao W, Xu H, Chu L, Bando Y, Golberg D, Eda G 2015 Appl. Mater. Today 1 60−66
[51] Lee Y H et al 2013 Nano Lett. 13 1852−1857
[52] Choi S H, Boandoh S, Lee Y H, Lee J S, Park J H, Kim S M, Yang W, Kim K K 2017 ACS Appl. Mater. Interfaces 9 43021−43029
[53] Zhang Y et al 2015 Nano Res. 8 (9) 2881−2890

Accepted Manuscript